The EMBO Journal vol.8 no.12 pp.3563-3570, 1989

Adenovirus polypeptide IX revealed as capsid cement by difference images from electron microscopy and crystallography

Paul S.Furcinitti[1,4], Jan van Oostrum[2,5] and Roger M.Burnett[3*]

[1]Biology Department, Brookhaven National Laboratory, Upton, NY 11973, [2]Department of Biochemistry and Molecular Biophysics, Columbia University, New York, NY 10032 and [3]The Wistar Institute, 3601 Spruce Street, Philadelphia, PA 19104, USA

[4]Present address: Biophysics Research Division, University of Michigan, Ann Arbor, MI 48109, USA
[5]Present address: Department of Biotechnology, CIBA-GEIGY AG, CH-4002 Basel, Switzerland

*Reprint requests[3]

Communicated by L.Philipson

Particles of adenovirus type 2 (ad2), when disassembled, consistently yield groups-of-nine (GON) hexons, which are the major virion shell component. The location of a minor component (6%) of the GON has been determined using a novel combination of electron microscopy and X-ray crystallography. The Brookhaven Scanning Transmission Electron Microscope (STEM) was used to estimate the distribution of protein in the GON to a resolution of 15–18 Å. The relative hexon positions then were determined to within 1 Å using a model of the hexon derived from the X-ray crystal structure to search the STEM image. The difference image between the STEM image and a model hexon group reveals individual monomers of polypeptide IX extending along the hexon–hexon interfaces. The distribution confirms our earlier proposal that four trimers of polypeptide IX are embedded in the large cavities in the upper surface of the GON to cement hexons into a highly-stable assembly.

Key words: adenovirus polypeptide IX/difference imaging/group-of-nine hexons/scanning transmission electron microscopy (STEM)/X-ray crystallography

Introduction

Polypeptide IX (14 339 daltons) (Aleström *et al.*, 1980) is one of at least 10 different structural proteins forming the virion (148.7 Md) (van Oostrum and Burnett, 1985) of human adenovirus. It is a minor component of the planar groups-of-nine hexons (GONs) that form the central region of each facet of the icosahedral adenovirus capsid and that are released on dissociation of the virion under mild conditions (Smith *et al.*, 1965; Laver *et al.*, 1969; Prage *et al.*, 1970) (Figure 1). The GON is 'propeller-shaped' and is left-handed when viewed from outside the virion (Pereira and Wrigley, 1974). Dissociation of the GONs themselves produces a pairwise pattern in which groups of seven, five and three predominate (Pereira and Wrigley, 1974). Recent results show polypeptide IX to be essential for packaging full-length viral genomes (Ghosh-Choudhury *et al.*, 1987).

The three-dimensional crystal structure of hexon, the major component of the capsid and of the GON, has been determined to 2.9 Å resolution (Roberts *et al.*, 1986). Hexons (3 × 109 077 daltons) have a pseudo-hexagonal base and a trimeric top, and form a small $p3$ net on each capsid facet with their 3-fold symmetry axis normal to the facet. Since the vertices of the triangular top of hexon are rotated by ~10° with respect to the pseudo-hexagonal base, the GON contains four large and three small cavities when the hexons are close packed (Burnett, 1985; van Oostrum *et al.*, 1987).

The original suggestion that polypeptide IX stabilizes the capsid (Maizel *et al.*, 1968) was confirmed by Colby and Shenk (1981) who showed that a mutant of ad5, containing a deletion in the gene for polypeptide IX, produced virions that are more heat-labile than wild-type and do not form GONs when dissociated. This indicates that, as polypeptide IX is not required for viral assembly, it probably is a capsid 'cement'. Burnett (1984) suggested that trimers of

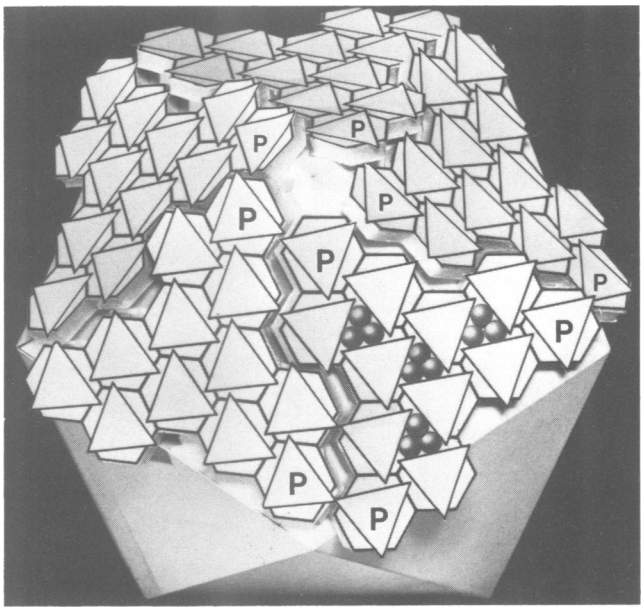

Fig. 1. A model of the icosahedral adenovirus capsid showing the organization of the major coat protein, hexon and the location of the capsid cement. Hexon is represented as a triangular top superimposed on a hexagonal base (see Figure 7). Each of the 20 capsid facets is formed from 12 hexons (polypeptide II). The penton complex between fiber (polypeptide IV) and penton base (polypeptide III) lies at each of the 12 vertices (complex not shown in the model). Polypeptide IX, represented as a sphere, binds in the central cavity between the towers of three different hexon molecules and in the three symmetry related locations elsewhere in the facet. Upon dissociation, the penton complex is lost from the 12 vertices of the icosahedron. The peripentonal hexons (P) surrounding each penton base are not cemented into the facet and are free to dissociate independently. Polypeptide IX stabilizes the central nine hexons so that they dissociate as an independent planar entity, the GON, which subsequently has a dissociation pattern reflecting the presence of the cement. Illustration from Burnett *et al.* (1990).

polypeptide IX are in the four large cavities in the GON. This idea is supported by stoichiometric measurements, which show there are 12 copies of polypeptide IX per GON and 240 per virion (van Oostrum and Burnett, 1985), and could explain both the non-random dissociation pattern of the GONs and the anomalous separate release of peripentonal hexons (Figure 1).

Our goal was to provide direct structural evidence for the idea, using the scanning transmission electron microscope (STEM) both to measure the molecular mass of GONs and to image polypeptide IX. The original plan was to form planar arrays of hexons without polypeptide IX (van Oostrum *et al.*, 1986) and compare these with GONs using unstained, freeze-dried specimens. Unfortunately, planar arrays did not form under the STEM preparation conditions and the GONs shrank on freeze-drying. In a revised experiment, GONs were completely embedded in negative stain and examined in the STEM. Their images showed no evidence of shrinkage, and revealed hexons whose density distribution correlated with the projected density of the 6 Å X-ray structure of hexon (Burnett *et al.*, 1985). The latter therefore was used to ascertain the relative positions of the individual hexons.

Results

Mass determination

GONs were freeze-dried and left unstained for molecular mass determination (Hainfeld *et al.*, 1982). Figure 2 shows a typical field of GONs with a tobacco mosaic virus (TMV) particle used as an internal mass standard. Freeze-dried GONs shrank more (17%) than the TMV standard (2−10%), original sizes being estimated from negatively stained examples or calculated from the hexon X-ray model (van Oostrum *et al.*, 1987). The unusually severe shrinkage of the GON was probably due to its unusually open structure, which arises from the cavities within the hexon bases on its lower surface and the gaps between neighboring hexon towers on its upper surface. Evidence for lateral movement of protein to fill these cavities was provided by contoured plots of the projected protein mass for individual examples (not shown). The central holes in individual hexons are clearly visible in stained examples, but absent in freeze-dried GONs (cf. Figures 2 and 3). The molecular mass was measured for both unfixed and glutaraldehyde-fixed GONs but the data were pooled as no difference in mass due to fixation was detectable by a two-tailed Student's *t*-test at the 99% level of significance. The pooled values for 323 GONs from 25 fields followed a Gaussian distribution with a mean mass of 3.11 ± 0.12 Md.

A two-tailed Student's *t*-test was used to evaluate the significance of the molecular mass determination. The value using the STEM is not significantly different at the 99% level from the value of 3.12 Md calculated from the stoichiometry and the molecular mass (van Oostrum and Burnett, 1985). The latter value was based on the relevant DNA sequences for GONs composed of 27 copies of hexon with mol. mass 109 077 daltons (Akusjärvi *et al.*, 1984), and 12 copies of

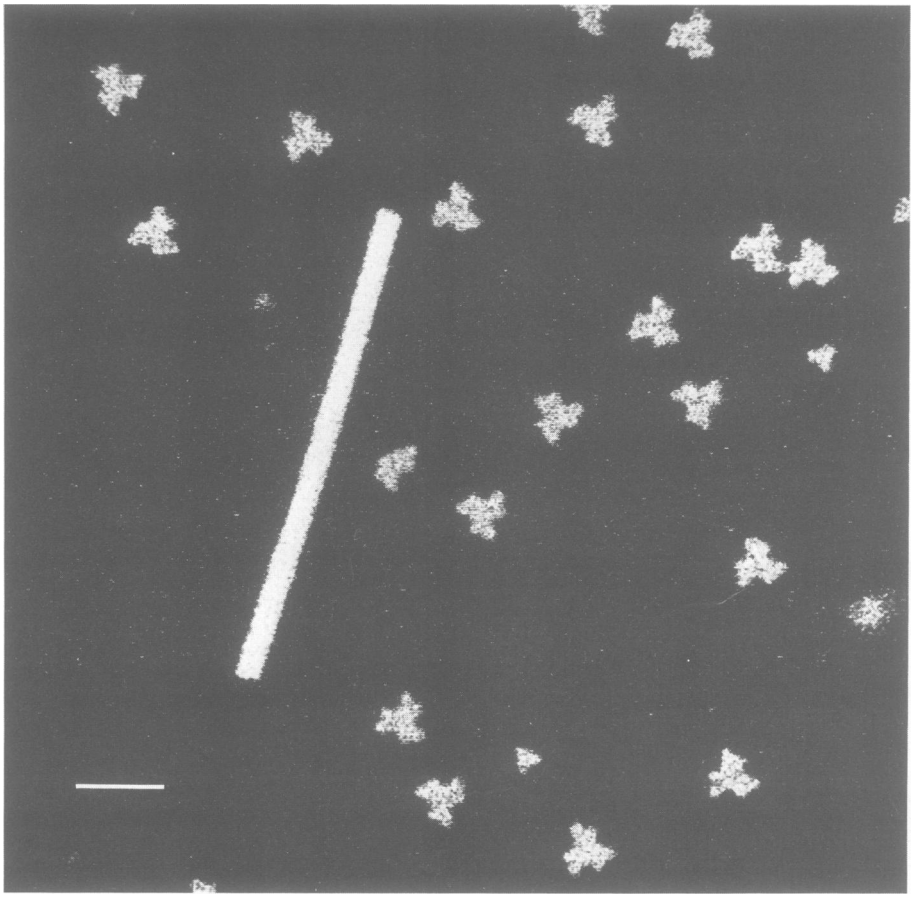

Fig. 2. Micrograph showing unstained, freeze-dried, GONs with a rod-shaped TMV particle as an internal mass standard, taken with the large-angle annular detector of the Brookhaven STEM. The image was obtained with 10 Å square pixels, at a dose of 8 e/Å^2. Scale bar equals 500 Å.

polypeptide IX with mol. mass 14 339 daltons (Aleström *et al.*, 1984; Roberts *et al.*, 1984), with both proteins acetylated at the N terminus. At the 99% level, the average of 323 values is not only significantly different from the mass of 2.95 Md for GONs with no polypeptide IX, but also differs from the masses of 3.07 and 3.16 Md estimated for GONs with either 9 or 15 copies of polypeptide IX. This degree of confidence results from the small standard deviation of the Gaussian mass distribution, which was obtained from a large number of individual measurements from several different grids. The molecular mass determined by the STEM is thus consistent with the proposed GON structure (Burnett, 1984). It is worth noting that the standard deviation of 4% in the mass measurements and the insignificant deviation from the calculated value place this mass determination as one of the most accurate yet performed (Wall and Hainfeld, 1984, 1986).

Image analysis of groups-of-nine

A typical field of negatively stained GONs is shown in Figure 3. The images of 102 GONs were selected interactively on a Lexidata 3400 display and the background value determined and subtracted from each image. The images of the few right-handed GONs were reversed so their images could be pooled with those of the predominating left-handed GONs (van Oostrum *et al.*, 1987). A low-pass filter (LP) with a resolution cutoff at 20 Å was applied to reduce the high-frequency noise in the images. The rotational power spectrum and a 3-fold rotationally filtered (RF) image were obtained for each image using programs written by Dr T.S. Baker (Purdue University), based on those of Crowther and Amos (1971). The best image (LP + RF) had 87% 3-fold symmetry, which was retained to 45 angular orders or 24 Å resolution. This was used as a reference image to which all other images were aligned using the SPIDER image analysis program system (Frank *et al.*, 1981a). The autocorrelation functions of the LP + RF images first were calculated to give centrosymmetric images that were rotationally aligned by angular cross-correlation. The rotations then were applied to the LP images before centering using a nine-point parabolic fit of the cross-correlation peaks.

The 65 images possessing >80% 3-fold symmetry were then submitted to correspondence analysis (Frank and van Heel, 1982; Frank, 1984) to select LP images with similar features. The approximately aligned LP images were multiplied by a mask to eliminate contributions from the surrounding support film. The mask was formed by superimposing all the aligned LP images, then setting all values outside the GON to zero and all values inside to one. A preliminary correspondence analysis showed that there were only three images >2.3 standard deviations from the mean. These were removed, a new correspondence map calculated, and a cloud of 30 images averaged to form a new reference image. This was both low-pass (20 Å) and rotationally

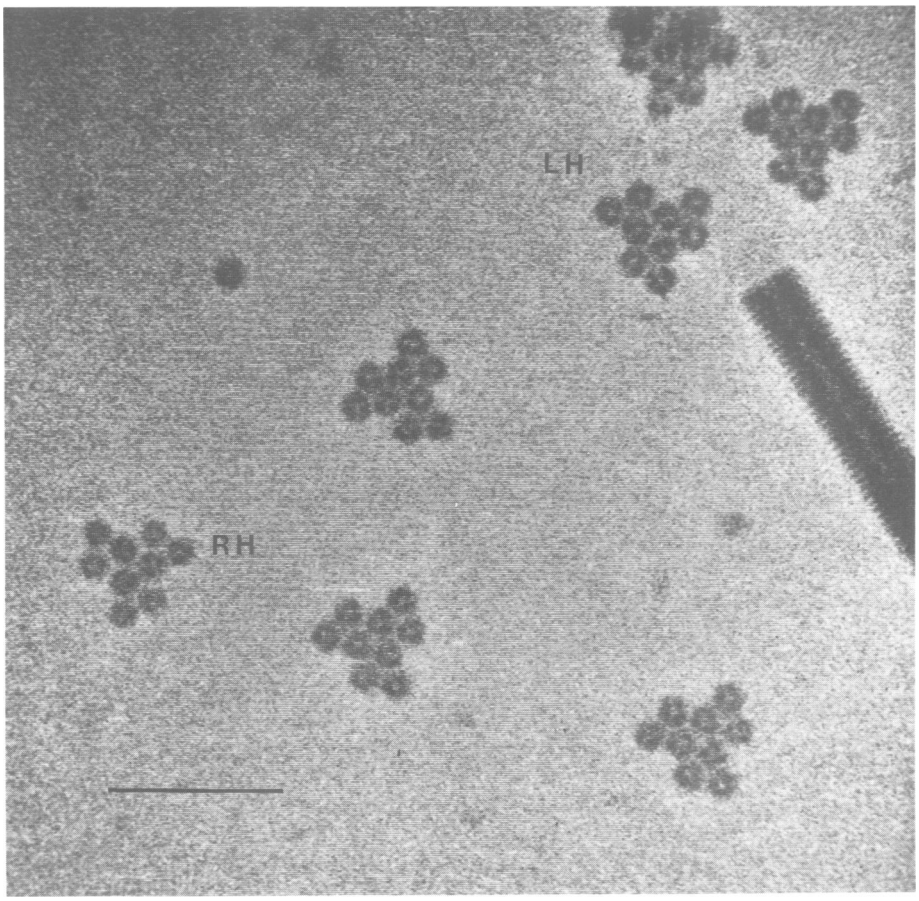

Fig. 3. STEM micrograph showing left-handed (LH) and right-handed (RH) GONs, and a representative TMV particle, fixed with glutaraldehyde and embedded in a thick layer of uranyl sulfate negative stain. The microscope was in Scherzer focus, and the image was obtained with the STEM large-angle annular detector, recording elastically scattered electrons. The image was taken with 5 Å square pixels at a dose of 12 e/Å^2. Scale bar equals 500 Å.

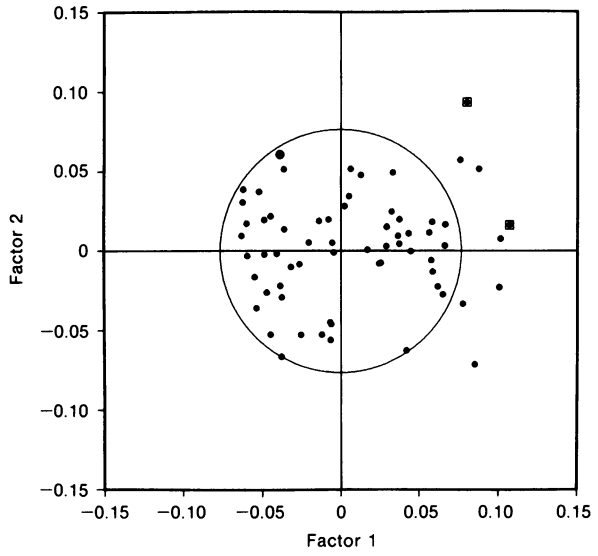

Fig. 4. Correspondence analysis map after the final alignment of 65 GONs with >80% 3-fold rotational power. The single example of an inverted right-handed GON (circled) could not be readily distinguished from left-handed GONs. Outliers from a previous correspondence analysis run were not used in the analysis (squares). The first eigenvector (horizontal axis) accounted for 11.8% of the total image variation, while the second (vertical axis) and third accounted for 5.7% and 4.6%. The 57 images in the large circle were averaged to form the final average.

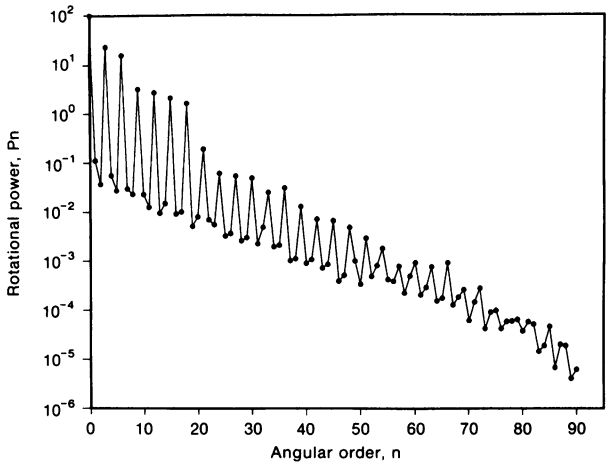

Fig. 5. Rotational power spectrum of the final average of 57 negatively stained GONs after low-pass filtration. The rotational power of each angular harmonic is scaled such that the coefficient of the zero order angular harmonic, P_0, is equal to 100.0. The 3-fold rotational symmetry is preserved to an angular order of 75, corresponding to a resolution of 15.1 Å with a GON radius of 185 Å, and accounts for 99.1% of the total angular power of the image.

filtered and used for accurate angular alignment of the approximately centered LP images. A final centering operation produced accurately oriented and centered images.

The realigned images were submitted to correspondence analysis to select the participants in the final average image. The outliers in the first factor map were removed, and a new map calculated (Figure 4). The 57 images circled in Figure 4 were included in the final average image, which was formed by superimposing the aligned unfiltered original images and low-pass filtering the average image to 12 Å

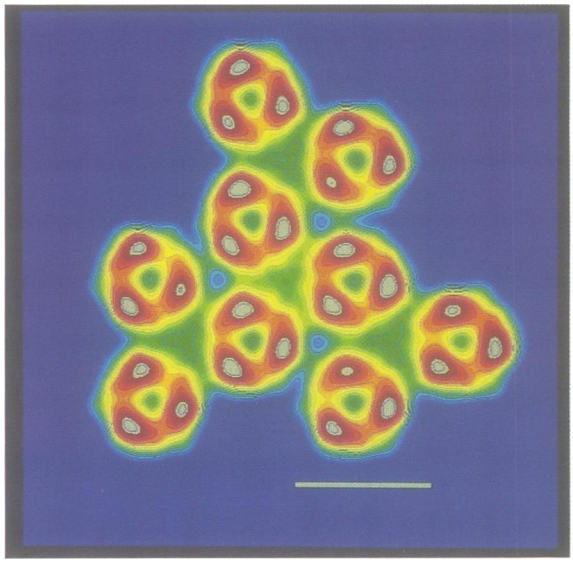

Fig. 6. Contour plot for the average of the 57 GON images selected from Figure 4, low-pass filtered to 12 Å, and rotationally filtered to retain 3-fold angular harmonics. Note the equivalent trimeric appearance of the three independent hexon images, and the four large and three small cavities between the hexons at the local 3-fold axes. The contours are in arbitrary units of projected protein mass and are colored from blue as a minimum through green, yellow and red, to grey as a maximum. Scale bar equals 100 Å.

Fig. 7. Model of the hexon trimer derived from the 6 Å X-ray electron density map. Each of the 29 slices in the model is 4 Å thick. Two distinct regions of the hexon are seen in the 6 Å model: a triangular 'top' 64 Å high that contains three towers; and a pseudo-hexagonal 'base' 52 Å high with a central cavity. The maximum radius of the hexon is 50 Å. The triangular top is rotated counterclockwise with respect to the pseudo-hexagonal base by ~10°.

resolution. The image was then rotationally filtered to determine its rotational power spectrum (Figure 5) and to produce a 3-fold symmetric average. The 3-fold symmetry

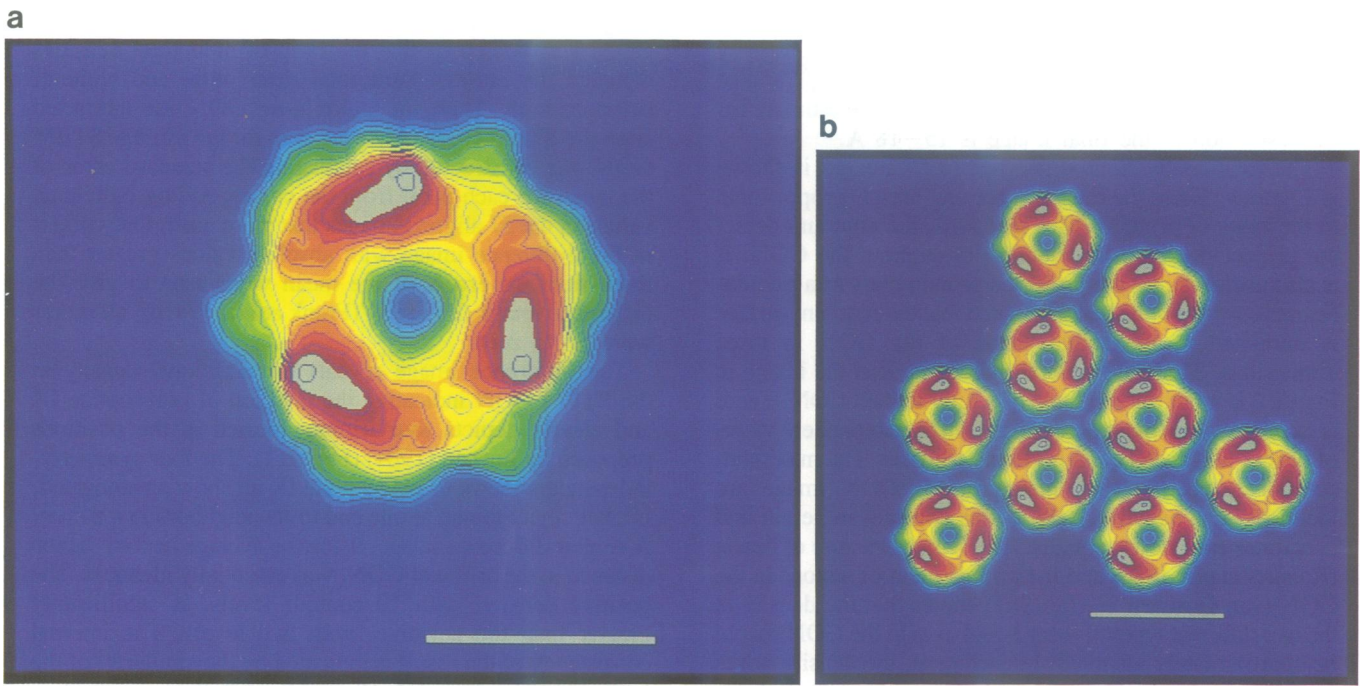

Fig. 8. (**a**) Contour plot for the hexon image derived as described in the text from the X-ray model shown in Figure 7. (**b**) An artificial GON constructed by placing nine copies of the X-ray hexon seen in (a) at the positions observed in the average GON image (Figure 6). Note the similar appearance of the GON in (b) and in Figure 6, except within the four large cavities between hexons. Scale bars equal 100 Å.

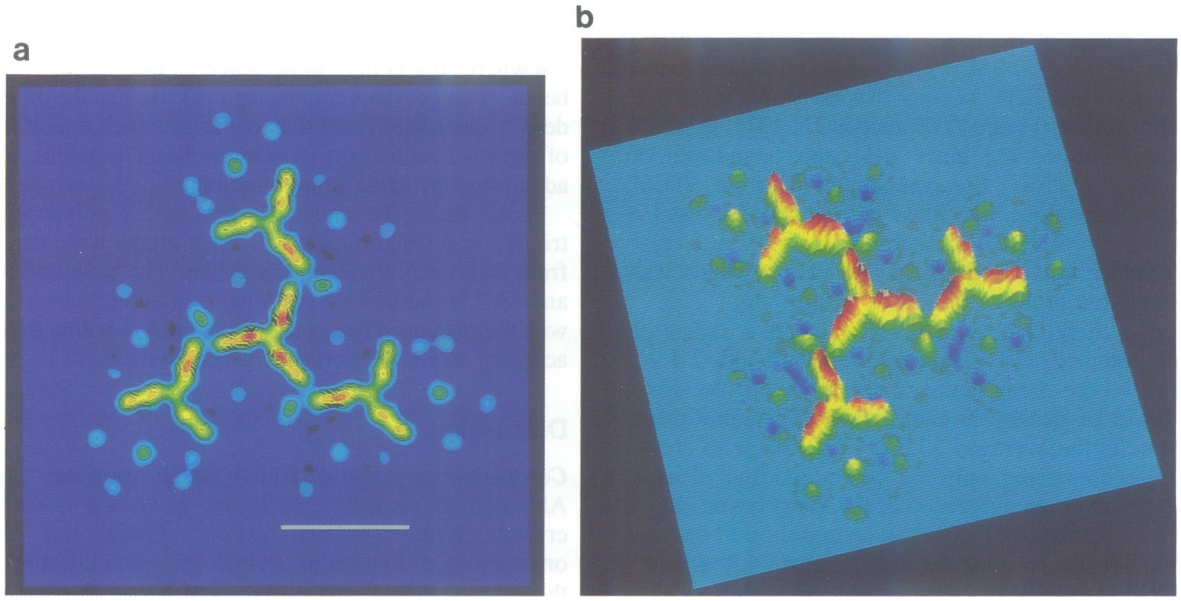

Fig. 9. (**a**) Contour plot of the significant difference image formed by subtracting the scaled artificial GON image of hexons alone (Figure 8b) from that of the STEM image of natural GONs containing both hexons and polypeptide IX (Figure 6). Only values greater than three standard errors of the mean were retained. Polypeptide IX is revealed as four trimers located in the large cavities between hexons and extending along the hexon–hexon interfaces. Scale bar in (a) equals 100 Å. (**b**) The difference image of the GON shown in (a) plotted with pseudo-height increasing with protein mass. Note that the viewing direction for this picture is the same as that for the cover illustration, but differs from that for the contour plots.

falls off noticeably beyond an angular order of 75, corresponding to a resolution of 15.1 Å for a GON with radius 185 Å, and is lost altogether at order 84 (13.5 Å).

An independent assessment of the resolution was made by calculating the differential phase residual (Unwin and Klug, 1974; Frank *et al.*, 1981b). The data set of 57 images was divided into two parts and the separate sets averaged, multiplied by a mask to exclude the peripheral stain region, low-pass filtered to a resolution of 12 Å, and rotationally filtered. The Fourier transforms of the masked averages were calculated and the differential phase residual determined as a function of resolution (not shown). The best-fit, cubic polynomial line drawn through the points indicates that the phase residual corresponding to 15.1 Å resolution is 57°. Following Frank *et al.* (1981b), who suggested that the limit of reproducible resolution corresponds to a phase residual

of 45°, a second estimate of the resolution achieved is 18.6 Å. It should be noted that this procedure necessarily reduces the signal-to-noise ratio by a factor of $1/\sqrt{2}$ and so provides a conservative estimate. A reasonable estimate for the resolution of the final image is 15–18 Å.

The rotationally filtered average of 57 images is shown in Figure 6. Since the intensity per unit area is proportional to the mass of protein above that area, the contours depict the projected protein distribution throughout the GON. It is also useful to plot the projected protein mass as a pseudo-height (cover), but it should be noted that the resultant surface is unrelated to the actual shape of the GON in three dimensions. There are several indications that the image in Figure 6 is a faithful rendition of a fully stained GON. There is excellent agreement between the three independent views of hexon, and each hexon is clearly trimeric. The maximum contour levels for each hexon in the GON image are identical. The negative stain is thus constant in height and penetrates each hexon equally. The X-ray structure of hexon (Roberts *et al.*, 1986) and the arrangement of hexons in the GON (van Oostrum *et al.*, 1987) shows that the density at the two different types of local 3-fold axes in the GON should be approximately identical. In each case, the density arises from three β-barrels of approximately equal height (Roberts *et al.*, 1986). However, Figure 6 shows additional contour levels in the four large cavities clearly demonstrating extra density at the postulated binding sites of polypeptide IX.

Construction of an artificial group-of-nine

The X-ray model of the hexon then was used as a probe within the averaged STEM image to determine the precise relationship of the GON hexons. An early model at 6 Å resolution was used (Figure 7) (Burnett *et al.*, 1985) in which envelopes delineated the inner and outer boundaries of electron density slices. For comparison with the STEM images, each envelope was filled with unit density and a summation performed in the direction of the 3-fold molecular axis to produce a two-dimensional projection, which was low-pass filtered to 15 Å resolution (Figure 8a).

A circular mask, with a value of unity, to a radius of 35 Å and a smooth Gaussian edge with halfwidth 2.5 Å, was drawn on the X-ray hexon image to include the three central peaks of density in each hexon. The same mask was applied to the averaged STEM GON image to create nine images containing only the central portion of each hexon. Angular cross-correlation of the X-ray hexon image with the nine masked STEM hexon images showed that the X-ray hexon must be rotated an average of 24.2 ± 0.9° counterclockwise to bring it into alignment with the GON hexons. Translational cross-correlation of the rotated X-ray hexon image with the STEM GON image produced nine peaks with an average hexon separation of 90.7 ± 1.2 Å, in good agreement with the value of 89 ± 5 Å reported by van Oostrum *et al.* (1987). Artificial GONs were then constructed either by placing the X-ray hexon model at the individually determined positions (Figure 8b) or by using the average hexon–hexon distance to form a $p3$ net (not shown). Figure 8(b) clearly shows that the density at the two different local 3-fold axes is very similar in the absence of polypeptide IX (cf. Figure 6).

Calculation of difference images

Difference images then were calculated. First, the averaged image of the STEM GON and that of the artificial X-ray GON were scaled so that the ratio of their total densities equalled the ratio of their total mass with, and without, polypeptide IX. Then, the scaled X-ray GON was subtracted from the STEM GON. An error map for the average STEM GON was constructed by calculating the standard error of the mean for each pixel from the corresponding individual values in the 57 aligned images that were used. Only pixels in the difference image with absolute values greater than three standard errors of the mean were used to give the difference image (Figure 9) (Frank *et al.*, 1981b), all others were set to zero.

The difference image reveals the additional density in the STEM GON indicating the position of polypeptide IX and clearly depicts four trimers located in the positions proposed by Burnett (1984) (Figure 1). The four symmetry-independent views of polypeptide IX all show an elongated, bilobal object joined at one end to its neighbors in a trimer. A similar difference image, using the average hexon–hexon distance in the artificial GON, was essentially identical. The positive density, with 10 contour levels, is significantly greater than the negative, with two levels. The internal consistency of the result is indicated by the similarity of the four views of polypeptide IX, and the excellent preservation of symmetry about the outer local 3-fold axes. It is particularly noteworthy that difference density is absent from the partial large cavities at the periphery of the GON (seen as blue indentations in the GON in Figure 6). The hexon–hexon interface at this location is chemically and topologically identical to that filled with polypeptide IX elsewhere, but is here unoccupied as the site lacks a third hexon. This provides convincing evidence that the difference density elsewhere is not due to artefacts such as contraction of negative stain upon irradiation (see Discussion for the advantages of using uranyl sulfate).

As a check, the molecular masses for polypeptide IX trimers in the significant difference image were estimated from their integrated intensity values. The values of 56 732 and 49 758 daltons for the inner and outer trimers agreed with the calculated mass (43 017 daltons) to within the rough accuracy expected from this procedure.

Discussion

Complementary use of STEM and X-ray data

Although the structure of hexon is known from X-ray crystallography (Roberts *et al.*, 1986), the relative orientations of hexons in crystals are quite different from those in the adenovirus capsid. The X-ray structure alone could not reveal the construction of the capsid but was the key to understanding adenovirus architecture when combined with information from electron microscopy (Burnett, 1984, 1985; van Oostrum *et al.*, 1987).

Crowther and Franklin (1972) pioneered the analysis of images of negatively stained GONs obtained in the conventional transmission electron microscope. Rotational filtration was used to show that hexons are arranged on a $p3$ net, rather than the $p6$ net predicted by the Caspar and Klug (1962) model of the adenovirus capsid as a hexamer-clustered $T = 25$ surface lattice. Their images had a resolution of ~56 Å, and individual images were not combined to form an average. Wrigley *et al.* (1982) used an optical 'flicker' method for angular and translational

alignment of noisy images of GONs to obtain average images confirming the $p3$ symmetry of GONs. Nermut (1975) obtained electron micrographs of GONs that distinguished between right- and left-handed views. The early micrographs were used by Burnett to assign the absolute orientation of the hexon trimer within the GON (Burnett *et al.*, 1979), and to develop a model for the placement of all hexons in the adenovirus capsid (Burnett, 1984, 1985). In more recent work by van Oostrum *et al.* (1987), the adenovirus capsid model was confirmed from different capsid fragments. In addition, right-handed GONs, lightly negatively stained to emphasize the upper surface, established the relative hexon positions in the GON to an accuracy of ~5 Å.

The work described in this paper using the STEM was far more precise (~1 Å). One factor undoubtedly was negative-staining with thick uranyl sulfate, which has a smaller grain size than other negative stains and is less likely to crystallize on exposure to electrons (Estis *et al.*, 1981). The use of this stain reduces problems associated with the contraction of negative stain upon electron irradiation, as seen for TMV stained with uranyl formate or acetate (Unwin, 1974). Probably as important was the large signal-to-noise ratio and the resolution of the STEM dark field image. Rejection of images with <80% 3-fold symmetry (Crowther and Franklin, 1972) was clearly useful as a criterion for selecting good images. Correspondence analysis was also an important tool in screening for similar images. However, only eight out of 64 left-handed GONs were excluded as dissimilar, and the solitary right-handed GON was shown to be as equally embedded as the left-handed GONs. This uniformity is in contrast to results obtained using light stain (van Oostrum *et al.*, 1987), where correspondence analysis separated the two hands. Finally, averaging was powerful in increasing the signal-to-noise ratio. The resolution of an individual image was observed as no better than 24 Å from its power spectrum, whereas the resolution of the final average lay in the range 15–18 Å.

Our results indicate that the resolution of negatively stained images and, more importantly, the faithful reproduction of biological macromolecules, may be greater than previously assumed. Two studies have shown that, at low resolution, images of negatively stained crystals of immunoglobulin G Dob (Steven and Navia, 1980) (20 Å) and lamprey lipovitellin complex (Raag *et al.*, 1986) (30–40 Å) agree with projections of their X-ray structures. Moreover, a recent comparison of negatively stained, frozen-hydrated and glucose-embedded specimens of ribosome crystals, bladder membrane and gap junctions (Milligan *et al.*, 1984) indicates substantial agreement among the structures at ~20 Å resolution, although negatively stained specimens were less similar at higher resolution. Although anionic and cationic stains give slightly different results (Baker *et al.*, 1985; Mannella *et al.*, 1986), this may not be a problem in difference imaging provided the same stain is used. Examples of small proteins visualized in larger assemblies include Soc of phage T4 (10 kd) (Ishii and Yanagida, 1975; Steven *et al.*, 1976; Aebi *et al.*, 1977), PD of lambda phage (11 kd) (Wurtz *et al.*, 1976) and trypsinized P10 of phage Φ29 connector (11 kd) (Carrascosa *et al.*, 1983).

The significant difference approach, which is available when several images are averaged, is powerful in rejecting spurious detail. Carrascosa and Steven (1978) used the standard deviation of the whole image as a threshold in determining where gp23 was cleaved (11 kd) in bacteriophage T4 capsids. We followed the approach of Frank *et al.* (1981b) who used the individual error of each pixel value in locating α-bungarotoxin molecules (8 kd) bound to two toxin-recognition sites on an acetylcholine receptor protein (Zingsheim *et al.*, 1982).

Polypeptide IX and virus stability

The results of the present structural investigation are consistent with earlier observations on polypeptide IX and GONs. The difference image shows that polypeptide IX is an elongated monomer with an axial ratio of 2.4, in approximate agreement with the value of 3.5 found by Lemay and Boulanger (1980) and consistent with its role as a capsid cement. The monomers bond pairs of hexons and cluster as four trimers within the large cavities of the GON, thus directly confirming the arrangement suggested by Burnett (1984) shown in Figure 1. The arrangement of polypeptide IX agrees with the stoichiometric determination (van Oostrum and Burnett, 1985), which found 12 copies within the GON and none elsewhere in the virion. The distribution of polypeptide IX explains the lack of attachment of the peripentonal hexons to the other hexons in the $p3$ facet, which leads to their anomalous separate release and the formation of GONs. The distribution also explains the non-random dissociation pattern of GONs (Pereira and Wrigley, 1974), the lack of reactivity of anti-IX antibodies to intact virions and the low antibody response to GONs (Cepko *et al.*, 1981). Polypeptide IX is an example of a class of proteins that has received little attention, but is important as it resolves conflicting demands for weak interactions during accurate assembly of multi-component systems and the strength required for their ultimate stability (Burnett, 1984).

Power of difference imaging

The difference imaging technique succeeded in locating polypeptide IX (14 339 daltons) between hexon pairs (654 462 daltons), a mass difference of only 2.2%. We conclude that the power of difference imaging has been underestimated previously. It is particularly useful when the images are accurate, care is taken with negative staining, and the specimen has internal symmetry. The use of correspondence analysis to average the STEM images gave a resolution of 15–18 Å. As the hexon model is known to much higher resolution (6 Å) than that used in the search (15 Å), we have confidence that the precision estimated from the hexon–hexon separation (90.7 ± 1.2 Å) is a measure of the accuracy in placement. Thus, the positions of hexons in the GON are determined to ~1 Å.

With the coordinates from the refined X-ray structure, and the constraints imposed when fitting together facets to form an icosahedral capsid, this study delineates the atomic positions of 62% of the protein in the ad2 virion (78.5 Md). We propose to extend the investigation to locate polypeptide VI (23 449 daltons), which remains attached to GONs under different experimental conditions (Everitt *et al.*, 1973). Subtraction of STEM images of the GON with, and without, polypeptide VI should reveal the location of this protein. We believe that the complementary use of X-ray crystallography with electron microscopy and image analysis will be of increasing importance in revealing the detailed organization of large macromolecular assemblies.

Materials and methods

Specimen preparation

GONs were isolated (van Oostrum and Burnett, 1985), and prepared for the STEM (Wall and Hainfeld, 1986) as described previously. They were further purified by molecular sieving through a Sepharose C1-4B column, equilibrated with 10 mM HEPES at pH 7.8, for accurate mass analysis. Particles of tobacco mosaic virus (TMV) (30 μg/ml) were used as an internal standard. They were injected (5 μl) into a drop of 20 mM ammonium acetate buffer at pH 7.0 upon a thin 'holey' carbon film supported by a titanium grid. The virus was attached for 2 min, and then washed several times with buffer. Ad2 GONs (32 μg/ml) were injected (2.5 μl) into the drop of buffer remaining on the film, attached for 1 or 2 min, washed eight times and freeze-dried. Some GON specimens were fixed in 0.1 or 0.5% glutaraldehyde for 2 min on ice before application to the carbon film. After freeze-drying (Mosesson *et al.*, 1981), specimens were warmed to room temperature and transferred under vacuum to the microscope. Negatively stained GONs were glutaraldehyde-fixed and attached for 2 min before the grids were washed six times with buffer and twice with a 2% solution of uranyl sulfate (Polysciences, Inc., Warrington, PA) (Estis and Haschemeyer, 1980). Excess stain was removed by capillary force from the grid, which was air-dried for ~45 s at room temperature.

Mass determination

Specimen imaging (Mosesson *et al.*, 1981) and mass measurement (Hainfeld *et al.*, 1982) were done using the signal from electrons elastically scattered through a large angle. Each microscope image, corresponding to the large-angle scattering signal, was displayed on a Lexidata 3400 monitor. The background value of the carbon support film was first evaluated as a smoothly varying function across the image. A conversion factor relating intensity to protein mass then was determined from the integrated, background-subtracted intensity for a TMV particle and its known mass per unit length. Finally, the mass of each freeze-dried GON was determined by integrating the intensity in a circular area containing a single GON, subtracting the corresponding background value, and multiplying by the conversion factor.

Acknowledgements

We thank Dr Harold S.Ginsberg, Dr Paul I.Freimuth and Ulla Lundholm for their assistance in purifying adenovirus particles. Particular thanks are due to Dr Joseph S.Wall for his support and advice while P.S.F. was a member of the STEM team at Brookhaven, to Kristin Elmore for sample preparation, and to Frank Kito for microscope operation. Dr Timothy S.Baker kindly helped in producing the color plates for publication. We are also indebted to Drs Carl W.Anderson, Adrian J.Gibbs, Paul V.C. Hough, Donatella Pascolini and Alisdair C.Steven for helpful criticism of the manuscript. The Brookhaven STEM Biotechnology Resource is supported by National Institutes of Health Grant RR 0177. Research support was also provided at the Brookhaven National Laboratory by the Office of Health and Environmental Research of the US Department of Energy. Most of the work by J.van O. and R.M.B. was done at Columbia University, under grants to R.M.B. from the National Science Foundation (DMB 84-18111 and DMB 87-21431) and the National Institute of Allergy and Infectious Diseases (AI 17270) and by an Irma T.Hirschl Career Scientist Award.

References

Aebi,U., van Driel,R., Bijlenga,R.K.L., ten Heggeler,B., van den Broek,R., Steven,A.C. and Smith,P.R. (1977) *J. Mol. Biol.*, **110**, 687–698.

Akusjärvi,G., Aleström,P., Pettersson,M., Lager,M., Jörnvall,H. and Pettersson,U. (1984) *J. Biol. Chem.*, **259**, 13976–13979.

Aleström,P., Akusjärvi,G., Perricaudet,M., Mathews,M.B., Klessig,D.F. and Pettersson,U. (1980) *Cell*, **19**, 671–681.

Aleström,P., Akusjärvi,G., Lager,M., Yeh-kai,L. and Pettersson,U. (1984) *J. Biol. Chem.*, **259**, 13980–13985.

Baker,T.S., Sosinsky,G.E., Caspar,D.L.D., Gall,C. and Goodenough,D.A. (1985) *J. Mol. Biol.*, **184**, 81–98.

Burnett,R.M. (1984) In Jurnak,F.A. and McPherson,A. (eds), *Biological Macromolecules and Assemblies. Vol. 1: Virus Structures*. Wiley, New York, pp. 337–385.

Burnett,R.M. (1985) *J. Mol. Biol.*, **185**, 125–143.

Burnett,R.M., Grütter,M.G., Markovic,Z. and White,J.L. (1979) *J. Supramol. Struct.*, **S3**, 92.

Burnett,R.M., Grütter,M.G. and White,J.L. (1985) *J. Mol. Biol.*, **185**, 105–123.

Burnett,R.M., Athappilly,F.K., Cai,Z., Furcinitti,P.S., Korn,A.P., Murali,R. and van Oostrum,J. (1990) In Laver,W.G. and Air,G. (eds), *Use of X-Ray Crystallography in the Design of Antiviral Agents*. Academic Press, San Diego, pp. 35–48.

Carrascosa,J.L. and Steven,A.C. (1978) *Micron*, **9**, 199–206.

Carrascosa,J.L., Carazo,J.M. and García,N. (1983) *Virology*, **124**, 133–143.

Caspar,D.L.D. and Klug,A. (1962) *Cold Spring Harbor Symp. Quant. Biol.*, **27**, 1–24.

Cepko,C.L., Changelian,P.S. and Sharp,P.A. (1981) *Virology*, **110**, 385–401.

Colby,W.W. and Shenk,T. (1981) *J. Virol.*, **39**, 977–980.

Crowther,R.A. and Amos,L.A. (1971) *J. Mol. Biol.*, **60**, 123–130.

Crowther,R.A. and Franklin,R.M. (1972) *J. Mol. Biol.*, **68**, 181–184.

Estis,L.F. and Haschemeyer,R.H. (1980) *Proc. Natl. Acad. Sci. USA*, **77**, 3139–3143.

Estis,L.F., Haschemeyer,R.H. and Wall,J.S. (1981) *J. Microsc.*, **124**, 313–318.

Everitt,E., Sundquist,B., Pettersson,U. and Philipson,L. (1973) *Virology*, **52**, 130–147.

Frank,J. (1984) *Ultramicroscopy*, **13**, 153–164.

Frank,J. and van Heel,M. (1982) *J. Mol. Biol.*, **161**, 134–137.

Frank,J., Shimkin,B. and Dowse,H. (1981a) *Ultramicroscopy*, **6**, 343–358.

Frank,J., Verschoor,A. and Boublik,M. (1981b) *Science*, **214**, 1353–1355.

Ghosh-Choudhury,G., Haj-Ahmad,Y. and Graham,F.L. (1987) *EMBO J.*, **6**, 1733–1739.

Hainfeld,J.F., Wall,J.S. and Desmond,E.J. (1982) *Ultramicroscopy*, **8**, 263–270.

Ishii,T. and Yanagida,M. (1975) *J. Mol. Biol.*, **97**, 655–660.

Laver,W.G., Wrigley,N.G. and Pereira,H.G. (1969) *Virology*, **39**, 599–605.

Lemay,P. and Boulanger,P. (1980) *Ann. Virol. Inst. Pasteur*, **131**, 259–275.

Maizel,J.V., Jr, White,D.O. and Scharff,M.D. (1968) *Virology*, **36**, 126–136.

Mannella,C.A., Ribeiro,A. and Frank,J. (1986) *Biophys. J.*, **49**, 307–318.

Milligan,R.A., Brisson,A. and Unwin,P.N.T. (1984) *Ultramicroscopy*, **13**, 1–10.

Mosesson,M.W., Hainfeld,J., Wall,J. and Haschemeyer,R.H. (1981) *J. Mol. Biol.*, **153**, 695–718.

Nermut,M.V. (1975) *Virology*, **65**, 480–495.

Pereira,H.G. and Wrigley,N.G. (1974) *J. Mol. Biol.*, **85**, 617–631.

Prage,L., Pettersson,U., Höglund,S., Lonberg-Holm,K. and Philipson,L. (1970) *Virology*, **42**, 341–358.

Raag,R., Roderick,S. and Banaszak,L. (1986) *J. Ultrastruct. Res.*, **94**, 77–84.

Roberts,R.J., O'Neill,K.E. and Yen,C.T. (1984) *J. Biol. Chem.*, **259**, 13968–13975.

Roberts,M.M., White,J.L., Grütter,M.G. and Burnett,R.M. (1986) *Science*, **232**, 1148–1151.

Smith,K.O., Gehle,W.D. and Trousdale,M.D. (1965) *J. Bacteriol.*, **90**, 254–261.

Steven,A.C. and Navia,M.A. (1980) *Proc. Natl. Acad. Sci. USA*, **77**, 4721–4725.

Steven,A.C., Couture,E., Aebi,U. and Showe,M.K. (1976) *J. Mol. Biol.*, **106**, 187–221.

Unwin,P.N.T. (1974) *J. Mol. Biol.*, **87**, 657–670.

Unwin,P.N.T. and Klug,A. (1974) *J. Mol. Biol.*, **87**, 641–656.

van Oostrum,J. and Burnett,R.M. (1985) *J. Virol.*, **56**, 439–448.

van Oostrum,J., Smith,P.R., Mohraz,M. and Burnett,R.M. (1986) *J. Ultrastruct. Mol. Struct. Res.*, **96**, 77–90.

van Oostrum,J., Smith,P.R., Mohraz,M. and Burnett,R.M. (1987) *J. Mol. Biol.*, **198**, 73–89.

Wall,J.S. and Hainfeld,J.F. (1984) In Bailey,G.W. (ed.), *Proc. 42nd Ann. EMSA Meeting*. San Francisco Press, San Francisco, pp. 154–157.

Wall,J.S. and Hainfeld,J.F. (1986) *Annu. Rev. Biophys. Chem.*, **15**, 355–376.

Wrigley,N.G., Chillingworth,R.K., Brown,E. and Barrett,A.N. (1982) *J. Micros.*, **127**, 201–208.

Wurtz,M., Kistler,J. and Hohn,T. (1976) *J. Mol. Biol.*, **101**, 39–56.

Zingsheim,H.P., Barrantes,F.J., Frank,J., Hänicke,W. and Neugebauer, D.-Ch. (1982) *Nature*, **299**, 81–84.

Received on June 23, 1989; revised on July 31, 1989